

Theoretical insights into the effect of halogenated substituent on the electronic structure and spectroscopic properties of the favipiravir tautomeric forms and its implications on the treatment of COVID-19

Letícia Cristina Assis,<sup>1</sup> Alexandre Alves de Castro,<sup>1</sup> João Paulo Almirão de Jesus,<sup>2</sup> Teodorico Castro Ramalho<sup>1</sup> and Felipe de Almeida La Porta<sup>2\*</sup>

<sup>1</sup> Department of Chemistry, Federal University of Lavras, CEP 37200-000 Lavras, Minas Gerais, Brazil

<sup>2</sup> Post-graduation Program in Materials Science and Engineering and Laboratory of Nanotechnology and Computational Chemistry, Federal Technological University of Paraná, Avenida dos Pioneiros 3131, 86036-370, Londrina, Paraná, Brazil.

\* [felipe\\_laporta@yahoo.com.br](mailto:felipe_laporta@yahoo.com.br) or [felipelaporta@utfpr.edu.br](mailto:felipelaporta@utfpr.edu.br)

**Abstract.** In this study, we systematically investigated the electronic structure, spectroscopic (nuclear magnetic resonance, infrared, Raman, electron ionization mass spectrometry, UV-Vis, circular dichroism, and emission) properties, and tautomerism of halogenated favipiravir compounds (fluorine, chlorine, and bromine) from a computational perspective. Additionally, the effects of hydration on the proton transfer mechanism of the tautomeric forms of the halogenated favipiravir compounds are discussed. Our results suggest that spectroscopic properties allow for the elucidation of such tautomeric forms. As is well-known, the favipiravir compound has excellent antiviral properties and hence was recently tested for the treatment of new coronavirus (SARS-CoV-2). Through in silico modeling, in the current study, we evaluate the role of such tautomeric forms in order to consider the effect of drug-metabolism into the inhibition process of the main protease ( $M^{pro}$ ) and RNA-dependent RNA polymerase (RdRp) of SARS-CoV-2 virus. These findings clearly indicated that all title compounds are better as RNA-inhibiting.

**Keywords:** Favipiravir; COVID-19; In silico modeling; Tautomers; Electronic structure; Spectroscopic properties

Considerable efforts have been performed in a short period of time in search of therapeutic options to treatment for infection caused by a new coronavirus – SARS-CoV-2 –, which is the cause of the disease called COVID-19.<sup>1-5</sup> Thus, researchers from all over the world have adopted as a strategy for treating COVID-19 infection attempt to inhibit two different types of known structural and non-structural proteins of the SARS-CoV-2 virus.<sup>6-10</sup> As such, the first case involves the inhibition of the main protease (abbreviated as M<sup>pro</sup>) proteins of SARS-CoV-2.<sup>9,11-14</sup> Notably, this structural M<sup>pro</sup> protein displays a pivotal role in the viral life-cycle due to their binding with the angiotensin-converting enzyme 2 (ACE2) receptor for the SARS-CoV-2 virus in host cells.<sup>9,11,15</sup> In contrast, after the SARS-CoV-2 virus enters into the host cell, it is well-known that the RNA-dependent RNA polymerase (abbreviated as RdRp), a non-structural protein, is the main enzyme for the process of SARS-CoV-2 replication.<sup>2,16-18</sup> Due to the eminent urgency to fight this COVID-19 outbreak, researchers around the world have widely evaluated the effectiveness of diverse approved antiviral agents for this proposed.<sup>1-3,19-21</sup>

Among these approved drugs, in particular, favipiravir (also known as T-705) is a compound analogous to guanine, which was developed with satisfactory activity against many RNA-polymerase viruses (e.g., Ebola, chikungunya, yellow fever, influenza, norovirus and enterovirus),<sup>22-27</sup> showed good clinical efficacy against coronavirus.<sup>28,29</sup> Although the highly mobile protons in the structure of favipiravir compounds has allowed for their tautomeric forms,<sup>30</sup> the interpretation of the spectroscopic properties of the tautomers has proven to be highly complex and difficult.<sup>31</sup> Their chemical structure and tautomeric form are shown in Figure 1.

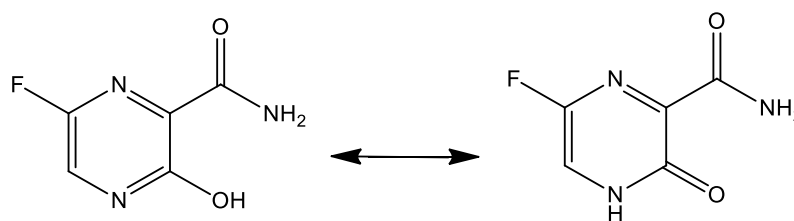


Figure 1. Chemical structure and tautomeric form of favipiravir.

Ongoing studies have focused on the understanding of the tautomeric forms of these compounds that are critically important for elucidating the nature of their chemical molecular

behaviour.<sup>30,31</sup> In contrast, quantum chemistry methods allow for the theoretical modelling of these spectral characteristics (i.e. to visualize this process on an atomic scale) quantitatively, which can, in principle, provide excellent opportunities for the design of new drugs.<sup>31-35</sup>

In this study, we focused on elucidating the effect of halide (fluorine, chlorine, and bromine) on the electronic structure, spectroscopic (nuclear magnetic resonance, infrared, Raman, electron ionization mass spectrometry, UV-Vis, circular dichroism, and emission) properties, and tautomerism of the favipiravir compounds from a computational perspective. In addition, since solvation has been known to play an important role in the tautomeric equilibrium,<sup>30-34</sup> the solvent effect was considered in the transition state calculations for the tautomerism of the isolated, mono-hydrate, di-hydrate and tri-hydrated forms of the different halogenated favipiravir compounds. Herein, we also used *in silico* modelling for predicting the possible effects of drug-metabolism in terms of action and toxicity for the halogenated favipiravir compounds against the SARS-CoV-2 using both M<sup>pro</sup> and RdRp sites as model systems.

In this *in silico* study, halogenated favipiravir tautomeric forms were firstly investigated by DFT and TDDFT calculations. Figure 2 (a-f) shows the optimized structures, bond lengths and ESP maps for each derivative. As seen in Figure 2, the change from F to Cl and Br atoms do not affect significantly the molecular structure, in general, except for the C-F to C-Cl and C-Br bond lengths, which are longer than expected (due to their higher atomic radius). However, the changes in the tautomer structures are mainly seen in the OH group, which shows longer C-O and shorter O-H bonds, though some shifts in the N-C and C-C bond lengths at the main ring are seen as well. Hence, it is well-known that such structural parameters are, in principle, dependents of the nature of bonded atoms and their chemical environment. Also, we observed an increase in the dipole moment with the replacement of fluoride in the favipiravir structures. Finally, all these parameters determined for the optimized structure are consistent with the literature.<sup>36,37</sup>

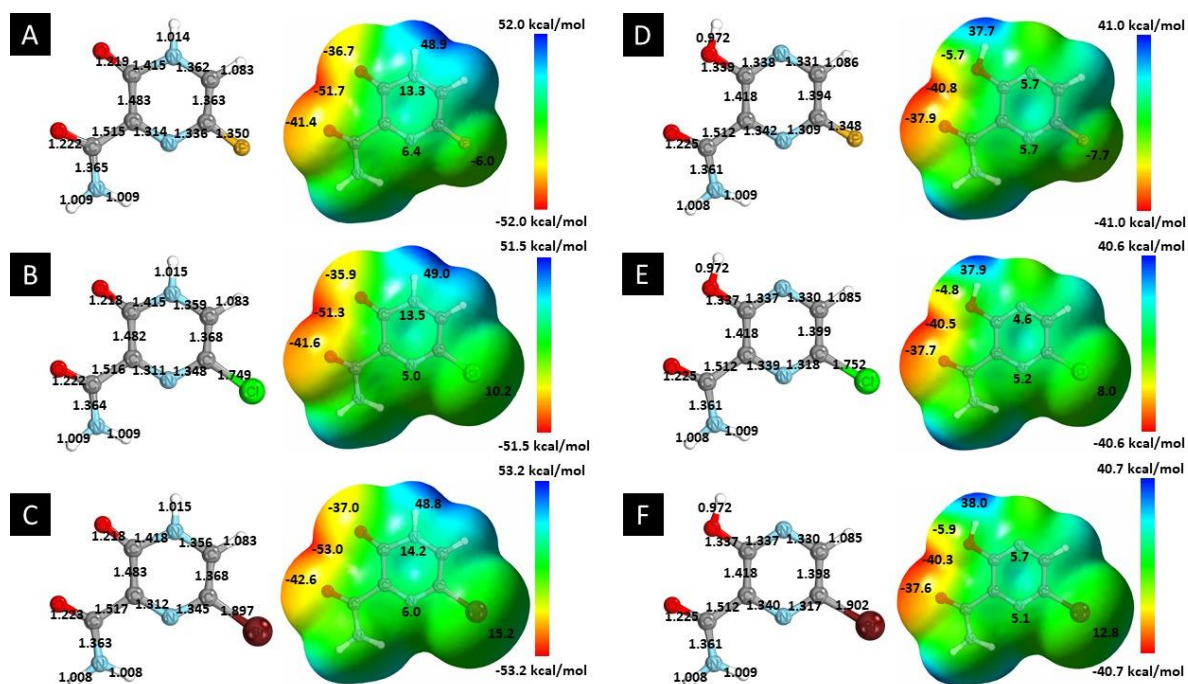
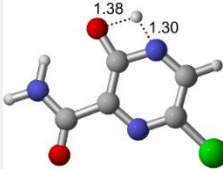
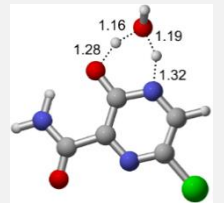
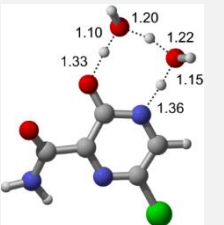
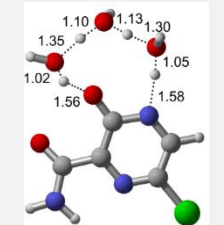
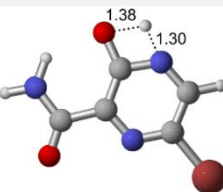
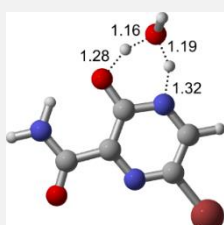
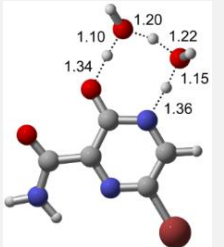
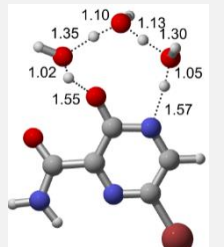
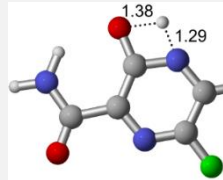
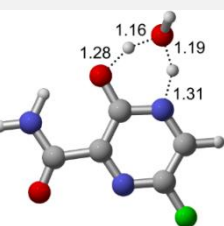
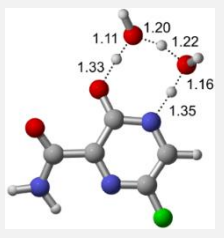
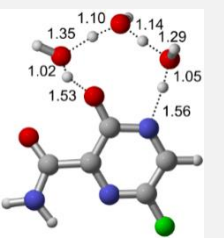
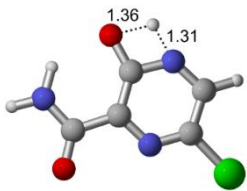
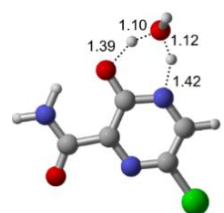
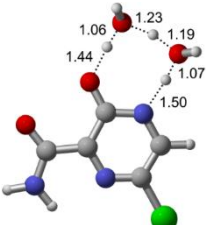
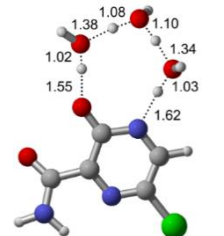


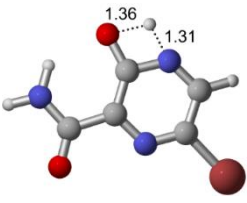
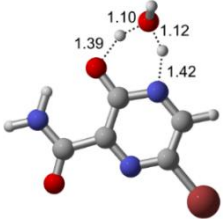
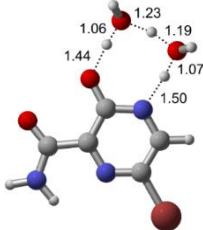
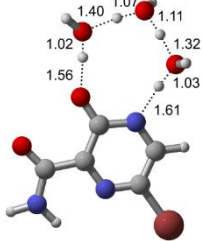
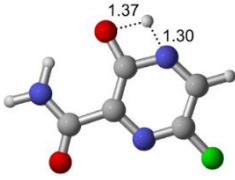
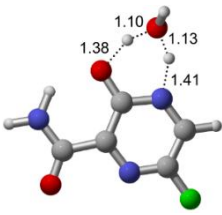
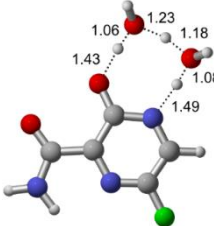
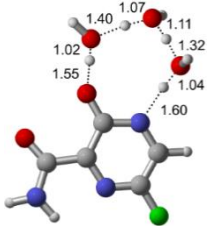
Figure 2. Optimized structures and ESP maps (with surface isovalue of 0.0004) for the halogenated favipiravir tautomeric forms: (a) 1-F; (b) 1-Cl; (c) 1-Br; (d) 2-F; (e) 2-Cl and (f) 2-Br. Image generated in the GaussView 6.0 <https://gaussian.com/gaussview6/>.

As for the ESP maps shown in Figure 2 (a-f), the charge distribution is oriented towards the O atoms and N-H or O-H functional groups for the derivatives. These high negatively (red) and positively (blue) charged surfaces, or respectively, electrons acceptor and donor areas, show the most favorable regions for interaction between molecules, thus having a higher reactivity.<sup>1,21</sup> As such, the halogenic substitution does not affect the charge distribution significantly; however, the tautomer molecules are lesser polarized than the original structure due to a charge stabilization in the O-H group.

According to Figure 1, the agent favipiravir undergoes a tautomerism process that gives rise to its tautomeric form. Hence, from a drug-metabolism perspective, this process occurs *via* a water-based proton transfer mechanism or without water-assisted. Hence, the TS obtained through DFT calculations for both cases are shown in Table 1. These calculations were carried out in gas phase and water as implicit solvent (PCM). In all cases, a single imaginary frequency was obtained as shown in Table 1, confirming the achievement of the TS.

Table 1. Transition states (TS) of the tautomerism mechanism of the water-assisted process and without water, in gas phase and implicit solvent (water), respectively. Image generated in the CYLview <http://www.cylview.org/>.

Gas phase					
Cl					
	Energy = -967.82 a.u. NIMAG = -1878.14 cm <sup>-1</sup>	Energy = -1044.31 a.u. NIMAG = -1453.72 cm <sup>-1</sup>	Energy = -1120.76 a.u. NIMAG = -1216.46 cm <sup>-1</sup>	Energy = -1197.21 a.u. NIMAG = -357.30 cm <sup>-1</sup>	
Br					
	Energy = -3079.35 a.u. NIMAG = -1877.99 cm <sup>-1</sup>	Energy = -3155.84 a.u. NIMAG = -1450.93 cm <sup>-1</sup>	Energy = -3232.29 a.u. NIMAG = -1214.20 cm <sup>-1</sup>	Energy = -3308.74 a.u. NIMAG = -355.42 cm <sup>-1</sup>	
F					
	Energy = -607.47 a.u. NIMAG = -1915.94 cm <sup>-1</sup>	Energy = -683.96 a.u. NIMAG = -1003.52 cm <sup>-1</sup>	Energy = -760.41 a.u. NIMAG = -1249.76 cm <sup>-1</sup>	Energy = -836.86 a.u. NIMAG = -417.01 cm <sup>-1</sup>	
Implicit solvent (water)					
Cl					
	Energy = -967.84 a.u. NIMAG = -1913.03 cm <sup>-1</sup>	Energy = -1044.33 a.u. NIMAG = -941.77 cm <sup>-1</sup>	Energy = -1120.79 a.u. NIMAG = -738.36 cm <sup>-1</sup>	Energy = -1197.24 a.u. NIMAG = -101.61 cm <sup>-1</sup>	

Br				
	Energy = -3079.37 a.u. NIMAG = -1913.72 cm <sup>-1</sup>	Energy = -3155.86 a.u. NIMAG = -930.60 cm <sup>-1</sup>	Energy = -3232.32 a.u. NIMAG = -744.43 cm <sup>-1</sup>	Energy = -3308.77 a.u. NIMAG = -133.15 cm <sup>-1</sup>
F				
	Energy = -607.48 a.u. NIMAG = -1915.94 cm <sup>-1</sup>	Energy = -683.98 a.u. NIMAG = -1003.52 cm <sup>-1</sup>	Energy = -760.44 a.u. NIMAG = -753.77 cm <sup>-1</sup>	Energy = -836.89 a.u. NIMAG = -139.32 cm <sup>-1</sup>

According to Table 1, the tautomeric mechanism without water molecules showed the highest TS energy, this is, less stabilizing energies. On the other hand, the water-assisted proton transfer mechanism led to more stabilizing TS geometries and decreased energies. We also can observe that by increasing the number of water molecules in the tautomerism process, it is possible to obtain more stable geometries for the TS structure, making this process energetically more favorable. Another important trend that should be highlighted is the fact of increasing the electronegative character of the atom directly bound to the ring (Br < Cl < F). Our findings show that the replacement of the chlorine atom from favipiravir with more electronegative atoms, such as fluorine, this leads to higher TS energy values. On the other hand, in case chlorine is replaced by a less electronegative atom, such as bromine, this feature leads to decreased TS energy values. According to these results, we can observe that there were no significant differences in energy for solvent calculations. However, structural changes can be noticed by the variation of distances among atoms.

Figure 3 (a) and (b) shows the infrared (IR) and Raman spectrum of title compounds. As a result, the 1-F derivatives present a main intense peak at 1802 cm<sup>-1</sup> related to the stretching of C=O groups and an important signal at 1312 cm<sup>-1</sup> assigned to the stretching of C-F, being blueshifted to 1170 cm<sup>-1</sup> and 1161 cm<sup>-1</sup> for Cl and Br, respectively. The peaks localized around 3590 cm<sup>-1</sup> and 3732 cm<sup>-1</sup> are related to, respectively, the symmetrical and asymmetrical stretchings of NH<sub>2</sub> and NH groups. As for the intense Raman signal at 1557 cm<sup>-1</sup>

<sup>1</sup>, it is characterized by the deformation of the aromatic ring by asymmetrical stretchings of N ring atoms. All peaks discussed for these structures are both IR and Raman active-modes, showing signals located at the same IR and Raman frequencies positions. the discussed signals are shifted from the 1-F molecules, thus the C=O stretching peak is blueshifted to 1770  $\text{cm}^{-1}$  and the C-F stretching to 1272  $\text{cm}^{-1}$ , however, the Cl and Br heteroatoms are redshifted to 1179  $\text{cm}^{-1}$  and 1172  $\text{cm}^{-1}$ , respectively. For the tautomers, it is noticed the appearance of significant peaks at 1489  $\text{cm}^{-1}$  and 3754  $\text{cm}^{-1}$ , associated, respectively, to C-O and O-H stretchings of OH group. It is worth notice that 2-F molecules present an intense IR active-mode around 330  $\text{cm}^{-1}$ , in which is related to the bending of  $\text{NH}_2$  group.

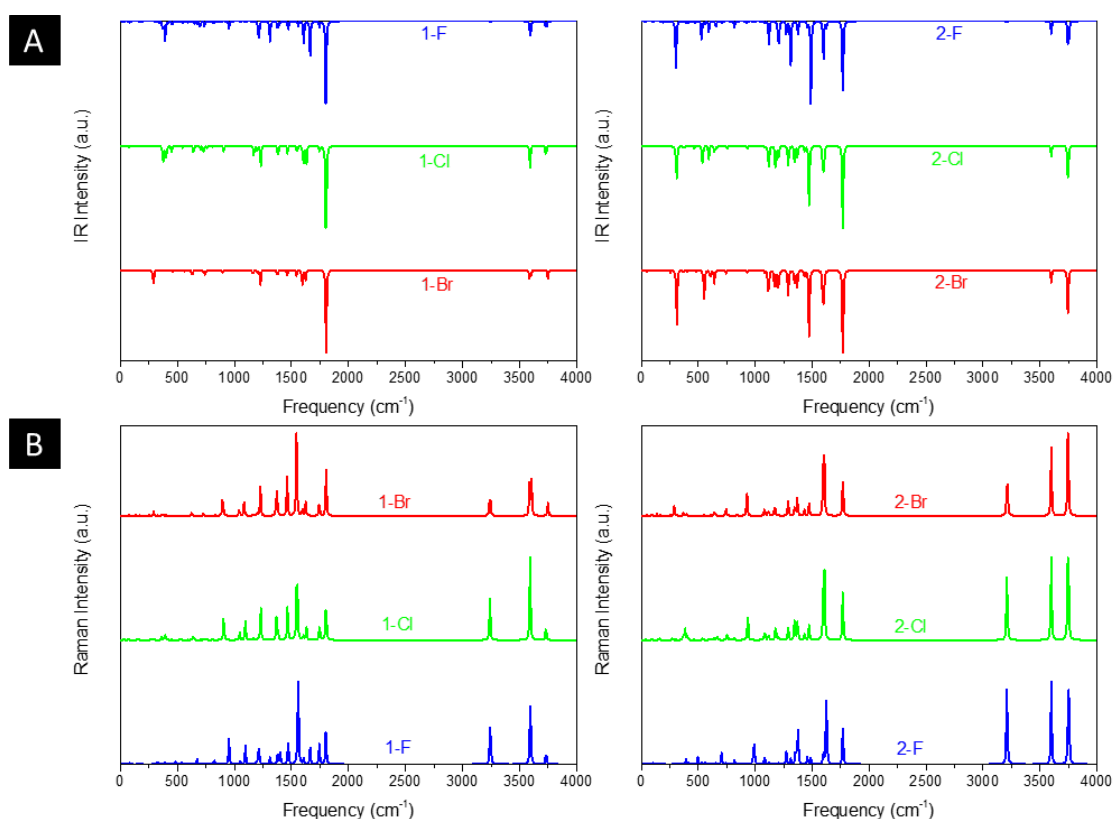


Figure 3. Computed (a) IR and (b) Raman spectra of the derivatives. Image generated in the Origin <https://www.originlab.com/>.

Figure 4 (a) and (b) illustrate the computed UV-Vis absorption and emission spectrum for the halogenated favipiravir compounds. For the UV-vis absorption spectrum of 1-F and 1-Cl derivatives, it is found an intense band at 350 nm and a very weak signal of high energy transition at 241 or 245 nm, respectively. In contrast, the 1-Br molecule shows only a small

redshifted for the most intense band, which is located at about 361 nm (see Figure 4 (a)). Note that the dotted line in Figure 4 (a) and (b) corresponds to the emission spectra for such compounds. From the emission and UV-vis absorption spectra of these compounds were calculated the Stokes shifts ranging from 76 nm (1-Br) to 104 nm (1-F). As it is shown, the lower energy part of the absorbance bands is overlapped with the higher energy part of the emission bands, forming a sensitive Förster Resonance Energy Transfer (FRET) region from intramolecular mechanisms.<sup>38</sup> As for the emission bands, it can be noted that a large peak at about 437 nm for both 1-Cl and 1-Br compounds. In contrast, we can observe a redshift in computed emission spectra for the 1-F compound, which have emission wavelengths at 454 nm. On the other hand, as shown in Figure 7 (b), the 2-F derivatives present only an intense band in the UV-vis absorption and emission spectra, with major blueshifts in the band position, ranging from 291 nm to 304 nm associated respectively to 2-F and 2-Br structures. The computed excitonic transitions, their related orbitals and the Stokes shifts for the halogenated favipiravir tautomeric forms are organized in Table 2.

Table 2. Analysis of UV-Vis and emission spectra of both 1 and 2 derivative tautomer forms.

Molecule	Excitonic transition	Absorbance wavelength	Emission	Emission wavelength	Stokes shift
1-F	HOMO → LUMO	350 nm	LUMO → HOMO	454 nm	104 nm
	HOMO-4 → LUMO	241 nm			
1-Cl	HOMO → LUMO	350 nm	LUMO → HOMO	437 nm	87 nm
	HOMO-4 → LUMO	245 nm			
1-Br	HOMO → LUMO	361 nm	LUMO → HOMO	437 nm	76 nm
2-F	HOMO-1 → LUMO	291 nm	LUMO → HOMO	312 nm	21 nm
2-Cl	HOMO-1 → LUMO	296 nm	LUMO → HOMO	319 nm	23 nm
2-Br	HOMO-2 → LUMO	304 nm	LUMO → HOMO	336 nm	32 nm

From Table 2, it is found that the excitonic transitions are mainly HOMO → LUMO for the 1-F type tautomers, while the 2-F type transitions happen from lower levels of the valence band to the LUMO orbital, as shown in Table 2. It is worth noticing that higher Stokes shifts of 1-F type derivatives may be a clue to a Excited States Intramolecular Proton Transfer (ESIPT).<sup>39</sup> In this framework, we propose from the higher Stokes shifts that the 1-F molecule and their halogenic species are part of an ESIPT mechanism, in which the excited 1-F molecules are quickly phototautomerized into excited 2-F derivatives due to a proton transfer between the aromatic N-H and its O=C neighbor, and returning to the original

structure by a reverse proton transfer after the radiative decay. However, as seen in the lower Stokes shifts, the same do not occur to the 2-F derivatives.

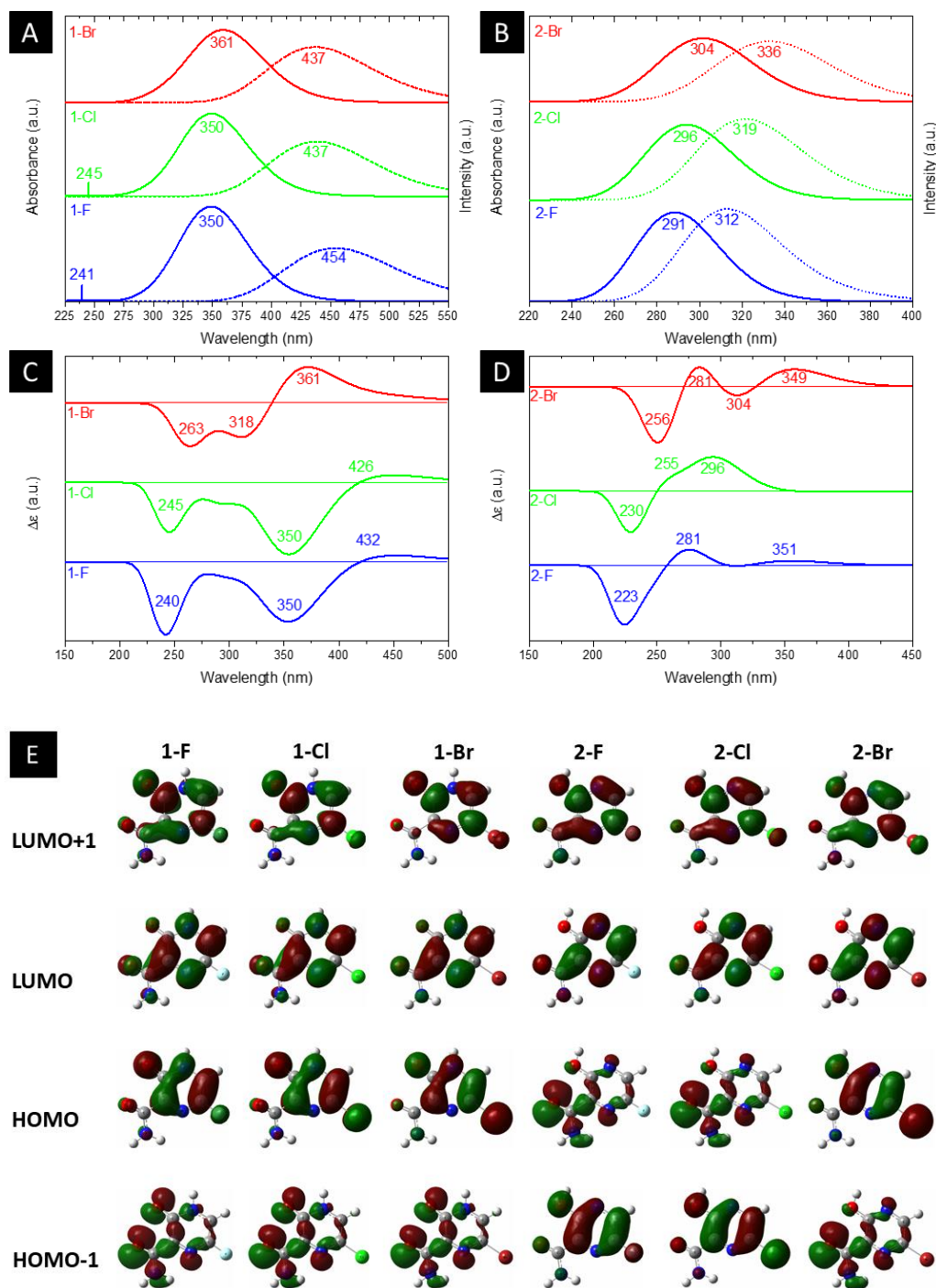


Figure 4. Computed (a and b) UV-Vis and emission, (c and d) ECD spectra and (e) MOs shapes (with a surface isovalue of 0.03) of both (a) 1 and (b) 2 derivative tautomer forms. Image generated in the GaussView 6.0 <https://gaussian.com/gaussview6/>.

Computed ECD data are also shown in Figure 4 (c) and (d). In the 1-F derivatives spectra, three signals are identified in the region between 220-440 nm, two being negatives (240-263 nm and 350-361 nm) and one positive (361-432 nm). As such, the 2-F and 2-Cl derivatives show three signals in the region of 200-360 nm, one negative (223-230 nm) and two positives (255-281 nm and 296-351 nm); however, there are four observed signals around 225-450 nm for the 2-Br tautomer, two being negatives (256 nm and 304 nm) and two positives (281 nm and 349 nm). Thus, it is analyzed that the change of heteroatom causes shifts in the positions and intensities of ECD signals, being the most significant modifications related to Br substitutions. Figure 4 (e) shows the LUMO+1, LUMO, HOMO and HOMO-1 shapes. From the HOMO and LUMO orbitals energies, the HOMO-LUMO gap and other electronic properties of the derivatives in their gas and water phase are calculated and organized in Table 3. Therefore, there are patterns in the HOMO-LUMO gaps, in which Cl derivatives have slightly higher energy and Br lower energy in comparison to their 1-F and 2-F tautomers. The HOMO-LUMO gaps are in accordance to the ESP maps as seen in Figure 2, which 1-F derivatives are more chemically reactive than 2-F due to their significantly smaller energy gaps. Along the energy gaps, other electronic properties are slightly shifted as well.<sup>37</sup>

Table 3. Electronic properties of the derivatives in gas phase and solution.

Molecule	Gas phase				
	HOMO-LUMO (eV)	Hardness (eV)	Softness (eV)	Mulliken Electronegativity (eV)	Electrophilicity (eV)
1-F	3.88	1.94	0.51	-5.02	50.40
1-Cl	3.91	1.95	0.51	-4.98	49.70
1-Br	3.83	1.91	0.52	-4.98	49.70
2-F	4.62	2.31	0.43	-5.02	50.40
2-Cl	4.64	2.32	0.43	-5.00	50.00
2-Br	4.58	2.29	0.44	-4.96	49.20
Molecule	Solution				
	HOMO-LUMO (eV)	Hardness (eV)	Softness (eV)	Mulliken Electronegativity (eV)	Electrophilicity (eV)
1-F	3.95	1.97	0.51	-4.87	47.53
1-Cl	3.98	1.99	0.50	-4.84	46.85
1-Br	3.89	1.94	0.51	-4.83	46.75
2-F	4.70	2.35	0.42	-4.96	49.2
2-Cl	4.67	2.33	0.43	-4.91	48.31
2-Br	4.59	2.29	0.44	-4.87	47.53

In addition, computed EI-MS spectrum were done as a mean to identify and differentiate each derivative and as well to understand their intermediary structures. Figure 5 shows the EI-MS spectrum and their respective trajectories, as well as intermediaries for all studied compounds. In every diagram is observed a peak at 44 m/z related to the linear group fragmentation outside the main ring of their source molecules. It is observed a pattern in the fragmentation of both F and Cl derivatives, in which the main structures are divided into two fragments, giving rise to signals related to a linear part (44 m/z) and a cyclic part with the heteroatom (113-129 m/z). However, it is observed a third peak at 80 m/z associated to Br atoms in the Br derivatives, as seen in Figure 5.

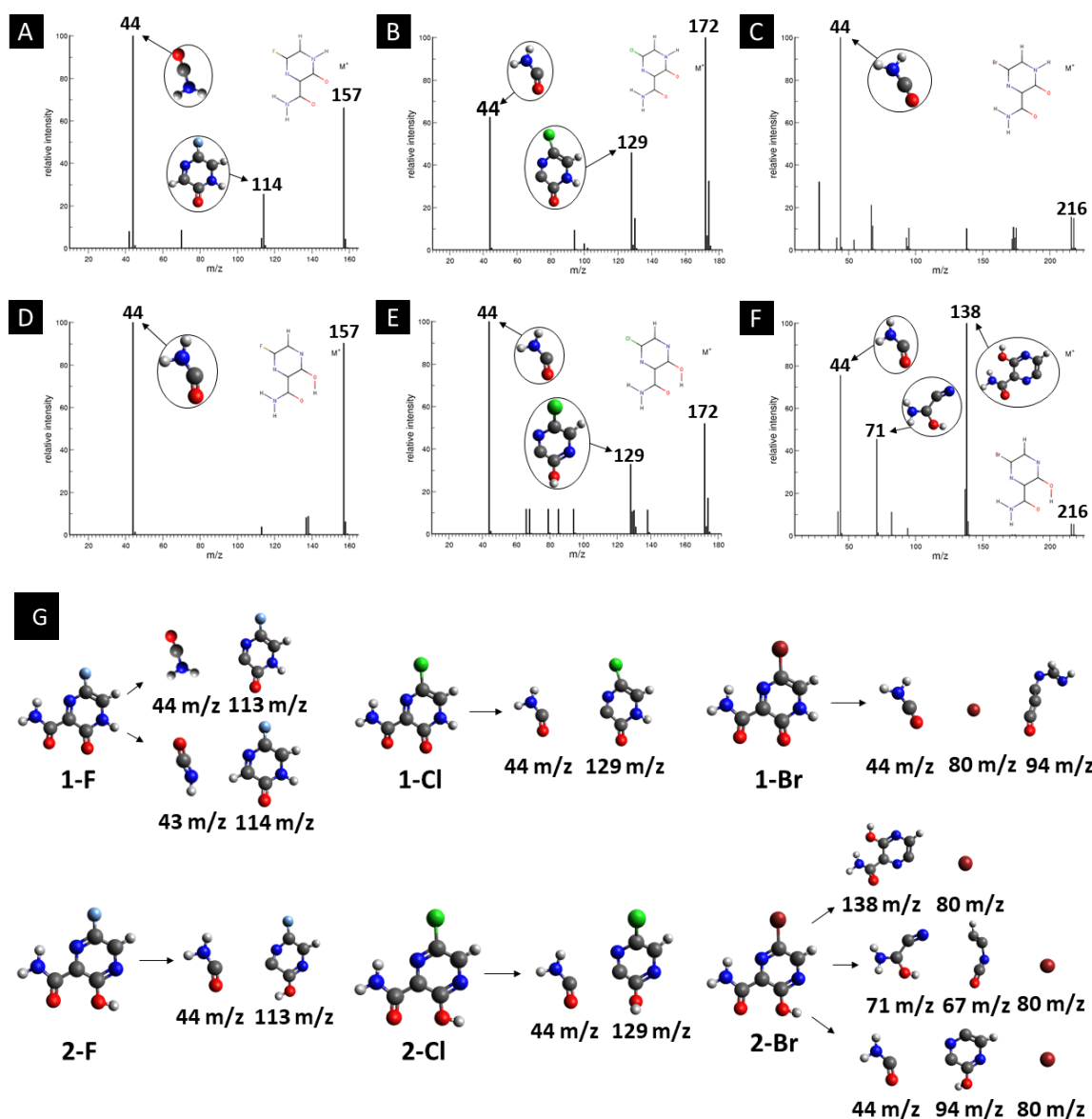
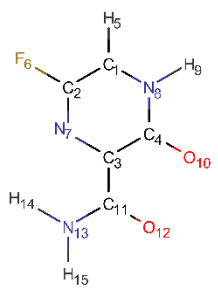
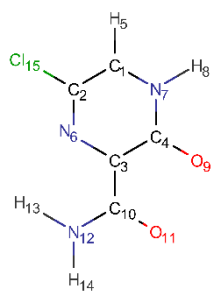


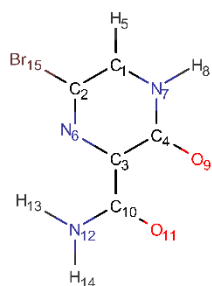
Figure 5. EI-MS diagrams, trajectories and intermediaries of all studied derivatives. (a) 1-F, (b) 1-Cl, (c) 1-Br, (d) 2-F, (e) 2-Cl and (f) 2-Br structures. Plots generated in the Grace

Software <https://plasma-gate.weizmann.ac.il/Grace/> and molecules in the Avogadro Editor <https://avogadro.cc/>

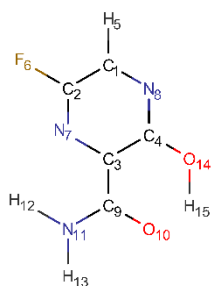
In order to best characterize the tautomers and understand their electronic structure, efforts have been made to obtain the NMR shieldings of the derivatives, as listing in Table 4. As such, the first is that N atoms next to the halogenic heteroatoms, and those close to OH group in the case the case of 2-F derivatives, present a relative lower shielding in comparison to other N atoms. Second, as the halogenic nuclei radius increases, the RNM shielding increases as well, ranging from 301.55 (F) to 2213.26 ppm (Br). The last conclusion to be made is that several shifts in the shieldings are observed when transitioning to solvent phase, as shown in the chemical shift  $\Delta\sigma$ , however, the chemical shift of  $O^{2-}$  nuclei are significantly higher than other nuclei. Hence, the main reason for these higher values is due to interaction between tautomers and water molecules from the solvent, in which hydrogen bonds are formed between HO-H molecules and C=O groups of the derivatives compounds.

Table 4. NMR shielding on nuclei of intermediaries in gas phase and in solvent water (PCM).

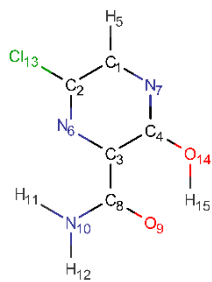
Molecule	Nuclei	Shielding in gas (ppm)	Shielding in water (ppm)	$\Delta\sigma$ (ppm)
 <p>1-F</p>	12-O	-66.26	-7.82	-58.44
	7-N	-44.26	-46.37	2.11
	10-O	-31.38	21.56	-52.94
	9-H	23.90	22.87	1.03
	5-H	24.68	24.05	0.63
	14-H	24.93	24.46	0.47
	15-H	27.08	26.61	0.47
	11-C	36.18	32.97	3.21
	4-C	48.12	44.99	3.13
	2-C	48.29	48.13	0.16
	3-C	51.00	53.71	-2.71
	1-C	79.01	73.18	5.83
	8-N	85.17	74.69	10.48
	13-N	171.85	165.03	6.82
6-F	301.55	303.73	-2.18	
 <p>1-Cl</p>	6-N	-67.44	-71.64	4.20
	11-O	-64.36	-7.16	-57.20
	9-O	-35.90	16.12	-52.02
	8-H	23.71	22.74	0.97
	5-H	24.62	24.04	0.58
	13-H	24.93	24.46	0.47
	14-H	27.10	26.64	0.46
	10-C	36.37	33.16	3.21
	4-C	48.75	45.66	3.09
	3-C	48.76	51.05	-2.29
	2-C	63.68	63.07	0.61
	1-C	66.99	61.93	5.06
	7-N	80.44	71.40	9.04



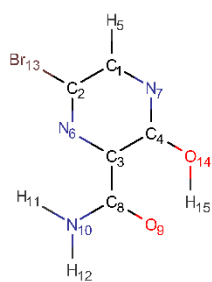
1-Br



2-F



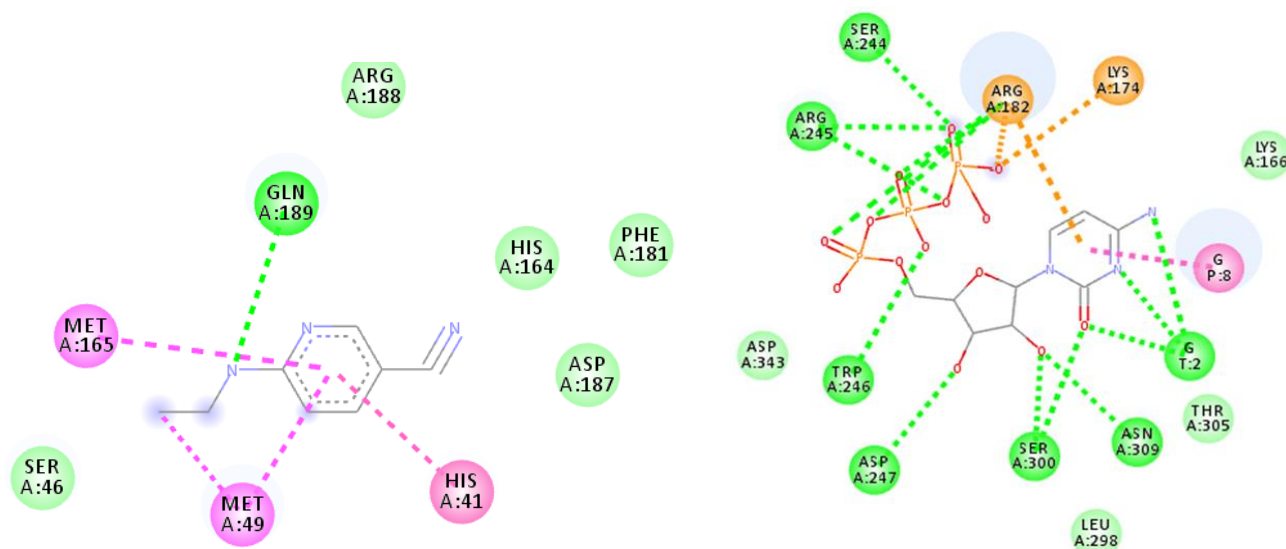
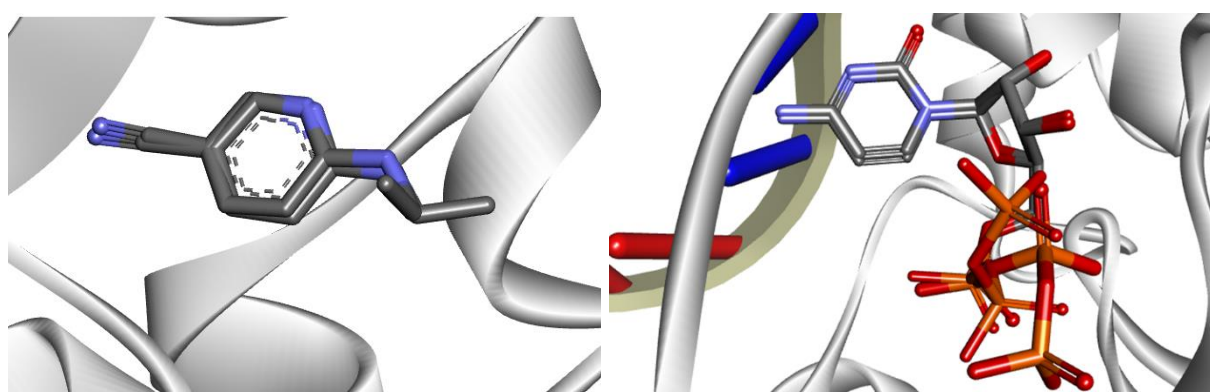
2-Cl



2-Br

12-N	172.46	165.63	6.83
15-Cl	708.05	709.13	-1.08
6-N	-73.15	-78.22	5.07
11-O	-66.76	-4.09	-62.67
9-O	-37.07	15.66	-52.73
8-H	23.61	22.67	0.94
5-H	24.46	23.91	0.55
13-H	24.60	24.13	0.47
14-H	27.06	26.61	0.45
10-C	37.34	34.27	3.07
4-C	49.03	45.73	3.30
3-C	50.48	52.34	-1.86
1-C	63.45	58.69	4.76
2-C	65.41	64.33	1.08
7-N	76.38	67.91	8.47
12-N	173.11	166.53	6.58
15-Br	2213.46	2212.032	-1998.57
10-O	-54.27	-4.43	-49.84
8-N	-47.51	-46.56	-0.95
7-N	-29.68	-28.50	-1.18
5-H	23.62	23.33	0.29
12-H	24.39	23.98	0.41
15-H	25.52	25.02	0.50
13-H	26.83	26.35	0.48
9-C	36.61	33.93	2.68
4-C	39.07	38.86	0.21
2-C	40.63	40.58	0.05
1-C	62.54	59.77	2.77
3-C	67.54	68.03	-0.49
11-N	170.19	163.66	6.53
14-O	190.07	196.21	-6.14
6-F	282.12	285.63	-3.51
6-N	-61.30	-60.84	-0.46
9-O	-52.74	-3.71	-49.03
7-N	-41.79	-40.70	-1.09
5-H	23.57	23.32	0.25
11-H	24.31	23.91	0.40
15-H	25.53	25.02	0.51
12-H	26.84	26.36	0.48
8-C	36.27	33.62	2.65
4-C	38.52	38.23	0.29
2-C	49.23	49.08	0.15
1-C	51.29	49.11	2.18
3-C	65.03	65.38	-0.35
10-N	169.91	163.55	6.36
14-O	189.35	195.18	-5.83
13-Cl	686.88	689.91	-3.03
6-N	-67.78	-67.52	-0.26
9-O	-52.47	-3.52	-48.95
7-N	-41.34	-40.11	-1.23
5-H	23.43	23.20	0.23
11-H	24.30	23.89	0.41
15-H	25.56	25.04	0.52
12-H	26.83	26.36	0.47
8-C	36.39	33.75	2.64
4-C	37.97	37.70	0.27
2-C	48.40	48.12	0.28
1-C	48.60	46.62	1.98
3-C	63.70	64.03	-0.33
10-N	170.51	164.07	6.44
14-O	189.30	195.14	-5.84
13-Br	2182.22	2185.65	-3.43

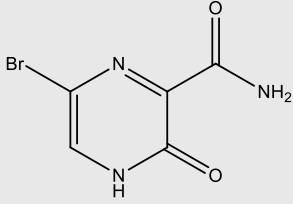
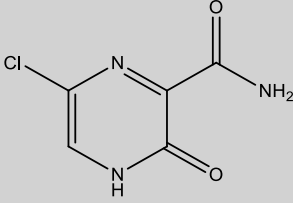
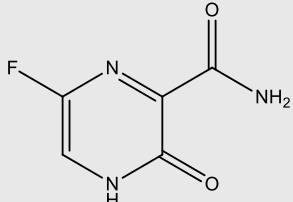
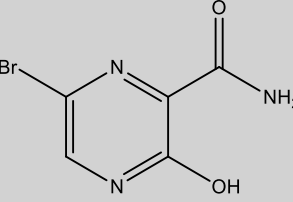
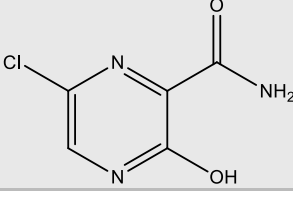
In order to analyze the interaction modes that our drug candidates performed with SARS-CoV-2, the crystal structures of the viral M<sup>pro</sup> in complex with 6-(ethylamino) pyridine-3-carbonitrile and RdRp polymerase in complex with cytidine-5'-triphosphate were downloaded from Protein Data Bank (PDB), codes 5R82 and 3H5Y, respectively.<sup>40,41</sup> As the enzymes were prepared, the molecular docking protocol was started. Thus, to evaluate the ability of the algorithm to predict possible ligand orientations, re-docking calculations were performed using the MolAr software,<sup>42</sup> with the implementation of the AutoDock Vina program.<sup>43</sup> As such, the values extracted from RMSD (5R82 = 0.94 Å / 3H5Y = 1.55 Å) indicated that Vina was able to predict the conformation that the co-crystallized ligands adopted experimentally within the SARS-CoV-2 M<sup>pro</sup> active site and SARS-CoV-2 RdRp

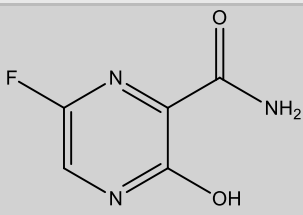


polymerase. Thus, the re-docking overlaps are shown in Figure 6. All computed interaction energy results are shown in Table 5.

Figure 6. Re-docking overlaps and representation of the interactions performed by co-crystallized ligand for SARS-CoV-2 M<sup>pro</sup> and SARS-CoV-2 RdRp sites. Interactions: green= Hydrogen bond, pink = hydrophobic and orange= coulombians. Image generated in the

Table 5. Intermolecular interaction energies obtained through Vina.

Compounds	Intermolecular interaction energy (kcal mol <sup>-1</sup> )	
	RdRp (PDB:3H5Y)	M <sup>pro</sup> (PDB:5R82)
 <p>1-Br</p>	-6.5	-4.4
 <p>1-Cl</p>	-6.5	-4.4
 <p>1-F</p>	-6.4	-4.8
 <p>2-Br</p>	-6.3	-4.6
	-6.3	-4.6

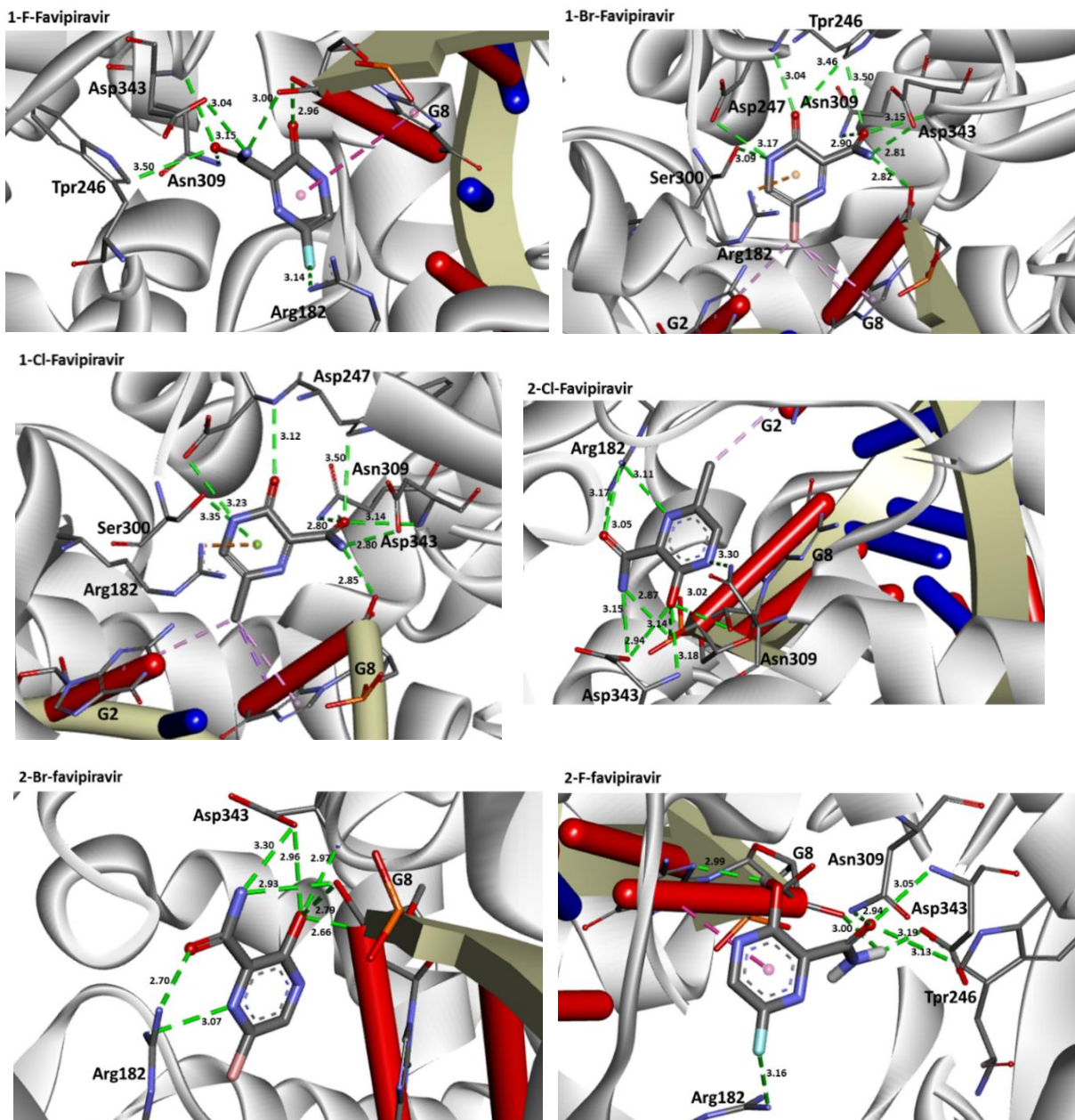
2-Cl		
	-6.3	-4.7
2-F		

According to Table 5, all drug candidates studied (i.e., favipiravir and its derivatives in both tautomeric forms) interacted well with the SARS-CoV-2 RdRp site, with interaction energy values in the range of -6.3 to -6.5 kcal mol<sup>-1</sup>, respectively. These studied compounds showed lower interaction energy values than the co-crystallized ligand (-3.5 kcal mol<sup>-1</sup>) within the SARS-CoV-2 RdRp site, indicating that these compounds are very promising for the inhibition of this molecular target. Regarding the M<sup>Pro</sup> enzyme, the studied compounds showed interaction energy values in a range of -4.4 to -4.8 kcal mol<sup>-1</sup>, respectively. However, these values were not lower than the co-crystallized ligand (-9.2 kcal mol<sup>-1</sup>). In general, it is noteworthy that the studied compounds had a good affinity within the active site of the molecular targets, but this class of compounds interacts better with the enzyme SARS-CoV-2 RdRp site.

Regarding interactions in the SARS-CoV-2 RdRp, the 1-Br and 1-Cl compounds showed the same interaction energy value, -6.5 kcal mol<sup>-1</sup>, being more stable than the other compounds, that is, they have settled very well in their place. Particularly, they performed hydrogen bonding interactions with Ser300, Asp247, Asp343, Trp246, Asn309, and G8, as well as Coulombian interactions with Arg182 and hydrophobic interactions with G2 and G8, respectively. It was also observed that these compounds interact with both the enzyme and RNA, remaining well accommodated in the 3H5Y site. These intermolecular interactions carried out by these compounds are important for the inhibition of this molecular target, and this can be corroborated by the interactions performed by the co-crystallized ligand at the 3H5Y site,<sup>40</sup> as shown in Figure 6.

In relation to the SARS-CoV-2 RdRp site, the compounds 2-Br, 2-Cl and 2-F had the same interaction energy value (-6.3 kcal mol<sup>-1</sup>), performing interactions with Arg182, Trp246, Asn309, Asp343, G8 and G2 (Figure 7). In this case, the Favipiravir compound presented energy of about -6.4 kcal mol<sup>-1</sup> and made interactions with Arg182, Trp246, Asn309, Asp343

and G8. A remarkable trend can be observed from these results, all tautomers (1-F, 1-Br and 1-Cl) showed better stability than their native forms (2-F, 2-Br and 2-Cl), that is, the tautomeric form of these compounds is very reactive at the SARS-CoV-2 RdRp site. Also, note that all of our drug candidates had key interactions for good affinity in the SARS-CoV-2 RdRp binding pocket, so we can suggest that favipiravir and its derivatives can effectively inhibit RNA polymerase, and in addition, being considered promising compounds for the



treatment of COVID-19.

Figure 7. Representation of the interactions performed by favipiravir and its derivatives in the SARS-CoV-2 RNA polymerase site. Image generated in the Discovery Studio Software 4.5 <https://discover.3ds.com/discovery-studio-visualizer-download>.

Regarding interactions at  $M^{pro}$ , it was observed that the compound favipiravir was the one that best interacted with this enzyme, with an intermolecular interaction energy value of around  $-4.8 \text{ kcal mol}^{-1}$ . As such, this compound performed two hydrogen bonds with His164 and Arg188, Coulombian with Cys145 and hydrophobic interactions with Met165 and His41, as well. It is worth mentioning, according to the literature,<sup>44</sup> that these residues are fundamental for inhibition of the viral  $M^{pro}$  (Figure 6 and 8). In the case of the 1-Br compound, in particular, was the one that least interacted at the  $M^{pro}$  active site in relation to the other compounds. According to our results, this compound performing interactions with Cys145, His41, Met49 and His154 (see Table 5). As shown in Figure 8, the other compounds also performed interactions with the aforementioned residues. It was observed that the tautomerism was not very significant for reactivity in this case. In general, our main objective was to determine whether the studied inhibitors could target the  $M^{pro}$  enzyme. The molecular coupling posture of each drug candidate indicated that they could, in fact, fit precisely in the substrate binding pocket.

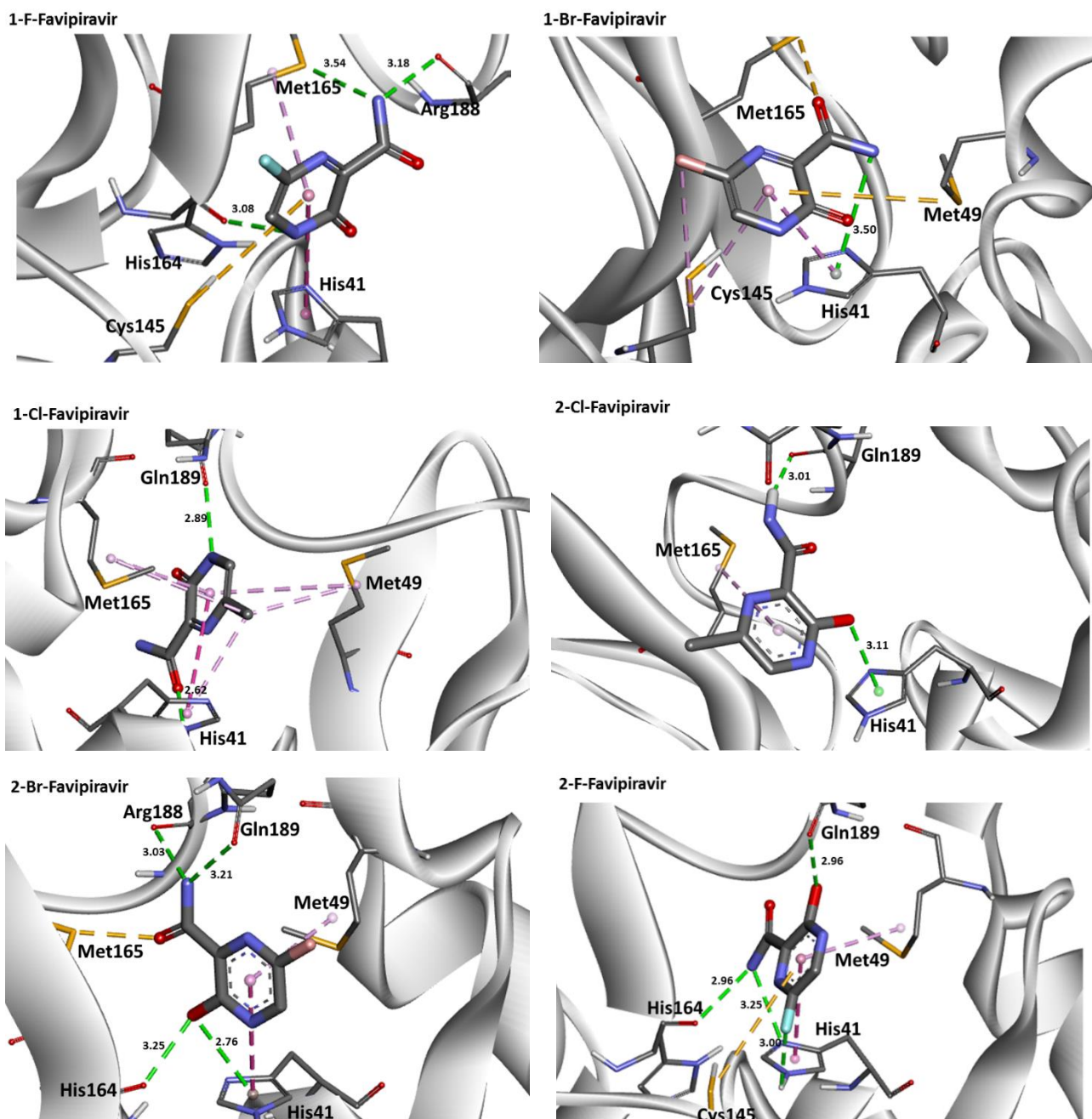


Figure 8. Representation of the interactions performed by favipiravir and its derivatives in the  $M^{pro}$  active site. Image generated in the Discovery Studio Software 4.5 <https://discover.3ds.com/discovery-studio-visualizer-download>.

Thus, in order to obtain theoretical of absorption, distribution, metabolism and excretion (parameters (LD50) were performed in ADMET, the results obtained for each compound are in Table 6. Lipinski's rule of 5 (RO5)<sup>45</sup> was used to evaluate the potential of these favipiravir derivatives as orally active drugs in humans, where it establishes that a molecule to be a good drug must present values for 4 parameters multiple of 5: log P greater

than or equal to 5, Molecular Mass less than or equal to 500, hydrogen bond acceptors less than or equal to 10 and binding donors hydrogen less than or equal to 5. We can note that the favipiravir derivatives violate the rules of maximum octanol/water partition coefficient. In addition, these compounds in their native form are more toxic than their tautomers and the halogens substitution have a significantly effect on the toxicity of these studied compounds. Therefore, these compounds have considerable drug potential.

Table 6. ADMET profile of selected favipiravir derivatives.

Comp.	MW	logP	D.H/ A.H	logS	Intestinal Absorption (%)	CNS	Tox. (LD <sub>50</sub> )
1-F	157.10	-0.99	2/3	-1.45	86.80	-3.06	1.92
1-Cl	173.56	-0.48	2/3	-1.94	87.00	-3.07	2.12
1-Br	218.01	-0.37	2/3	-2.03	86.95	-3.06	2.13
2-F	157.10	-0.58	2/4	-1.88	86.04	-3.12	1.52
2-Cl	173.56	-0.06	2/4	-2.29	86.59	-3.11	1.8
2-Br	218.01	0.04	2/4	-2.36	86.53	-3.11	1.81

Comp = Compounds favipiravir derivatives. ADME parameters: MW = molecular weight, D.H = number of Hbonds donors, A.B. = number of Hbonds acceptors, logP = partition coefficient, logS = predicted aqueous solubility, CNS = predicted central nervous system, Tox= Oral Rat Acute Toxicity (mol Kg<sup>-1</sup>).

In conclusion, we have studied the electronic structure and spectroscopic properties of halogenated favipiravir tautomeric forms. These results are compatible with reported theoretical-experimental data (when available), allowing for a complete distinction in both tautomeric forms. Therefore, in this study, these effects were evaluated in order to consider favipiravir and its metabolic derivatives, since this compound has recently been used for the treatment of COVID-19. All halogenated favipiravir tautomeric forms were investigated against the SARS-CoV-2 using both M<sup>pro</sup> and RdRp sites as model systems. Since all molecules have shown RNA-inhibiting properties, generating potential candidates for the COVID-19 treatment. Hence, we strongly recommend that future in silico studies address both biological targets, what could certainly contribute for the development of new therapies based on the combined use of drugs.

## COMPUTATIONAL DETAILS

Here, all quantum-chemical calculations were done through Gaussian 09 package.<sup>46</sup> Full optimization and their frequencies of halogenated favipiravir compounds (fluorine, chlorine, and bromine) were achieved with Density Functional Theory (DFT) method at the B3LYP/6-31+G(d,p) level. Then, in order to consider the effect of drug metabolism, the transition states (TS) for the tautomeric forms of title compounds were computed through DFT calculations, at the same level of theory described previously. Additionally, the solvent effect (water) was considered in the TS calculations for the tautomerism of the isolated, mono-hydrate, di-hydrate and tri-hydrated forms using the polarizable continuum model (PCM).<sup>47,48</sup> In addition, NMR calculations (in the gas phase and solution) were also performed for tautomeric forms of the halogenated favipiravir compounds at the B3LYP/6-31+G(d,p) level what do method.<sup>49-53</sup> Time-Dependent DFT (TD-DFT) calculations were also evaluated to obtain the UV-Vis, Electronic Circular Dichroism (ECD) and emission spectra, as well as their excitonic transitions, Molecular Orbitals (MOs) and Electrostatic Surface Potential (ESP) maps. Additionally, the Electron Ionization Mass Spectrometry (EI-MS) fragmentation spectrum for tautomeric forms and the trajectories of intermediaries were evaluated through semiempirical GFN2-xTB method as implemented in Quantum Chemistry Electron Ionization Mass Spectrometry program (QCEIMS).<sup>54,55</sup> The MarvinSketch software was used to draw the 2D chemical structures (<https://chemaxon.com/products/marvin>) and Avogadro software.<sup>56</sup>

The molecular docking was conducted with the tool AutoDock Vina (version 1.1.2),<sup>43</sup> as implemented in the MolAr (Molecular Architecture) software.<sup>42</sup> For the crystallographic M<sup>pro</sup> and RdRp polymerase structures preparation, the loop regions were rebuilt using the Modeller.<sup>57</sup> As such, the ions and water molecules were removed from the original PDB, with the exception of water molecules that were in the M<sup>pro</sup> and RdRp active sites. Additionally, the polar hydrogen atoms was added in Chimera software<sup>58</sup> according to the protonation state of the receptor at a pH value of 7.4. For the docking protocol, both M<sup>pro</sup> and RdRp enzymes and the structures of halogenated favipiravir tautomeric forms were used as receptor and ligands, respectively. Hence, the grid box was centered on the co-crystallized ligand (6-[ethylamino]pyridine-3-carbonitrile) of SARS-CoV-2 virus M<sup>pro</sup> enzyme (5R82), and the coordinates were  $x = 12.053$ ,  $y = -0.871$  and  $z = 24.157$ , with 1 Å spacing. As such, the same procedure was performed for the enzyme of SARS-CoV-2 RdRp polymerase, the grid box was centered on the co-crystallized ligand cytidine-5'-triphosphate (3H5Y), and the

coordinates were  $x = 30,594$ ,  $y = 0.628$  and  $z = -0.780$ , with about of 1 Å spacing. Finally, the docked poses obtained along in this procedure were then selected on the basis of scoring functions as well as protein–ligand interactions. Binding interaction figures were generated using Discovery Studio 2017 R2.<sup>59</sup> We also provide a theoretical estimation for the acute toxicity by use of LD<sub>50</sub> values obtained from a rat model-based admetSAR predictor, which is freely available online at <http://biosig.unimelb.edu.au/pkcsm/prediction>.

## ACKNOWLEDGEMENTS

The authors gratefully acknowledge the support from the Brazilian agencies CNPq, CAPES and FAPEMIG.

## REFERENCES

- (1) Assis, L. C.; Castro, A. A.; Jesus, J. P. A.; Nepovimova, E.; Kuca, K.; Ramalho, T. C.; La Porta, F. A. Nitro Derivatives of Quinoline and Quinoline N-Oxide as Low-Cost Alternative for the Treatment of SARS-CoV-2 Infection. Research Square 2020. <https://doi.org/10.21203/rs.3.rs-32468/v1>.
- (2) Li, G.; De Clercq, E. Therapeutic Options for the 2019 Novel Coronavirus (2019-NCoV). *Nature reviews. Drug discovery*. England March 2020, pp 149–150. <https://doi.org/10.1038/d41573-020-00016-0>.
- (3) Zhou, P.; Yang, X. Lou; Wang, X. G.; Hu, B.; Zhang, L.; Zhang, W.; Si, H. R.; Zhu, Y.; Li, B.; Huang, C. L.; et al. A Pneumonia Outbreak Associated with a New Coronavirus of Probable Bat Origin. *Nature* 2020, 579 (7798), 270–273. <https://doi.org/10.1038/s41586-020-2012-7>.
- (4) Campos, E. V. R.; Pereira, A. E. S.; de Oliveira, J. L.; Carvalho, L. B.; Guilger-Casagrande, M.; de Lima, R.; Fraceto, L. F. How Can Nanotechnology Help to Combat COVID-19? Opportunities and Urgent Need. *J. Nanobiotechnology* 2020, 18 (1), 125. <https://doi.org/10.1186/s12951-020-00685-4>.
- (5) Daré, J. K.; Silva, D. R.; Ramalho, T. C.; Freitas, M. P. Conformational Fingerprints in the Modelling Performance of MIA-QSAR: A Case for SARS-CoV Protease Inhibitors. *Mol. Simul.* 2020, 46 (14), 1055–1061.

<https://doi.org/10.1080/08927022.2020.1800691>.

- (6) Ton, A.; Gentile, F.; Hsing, M.; Ban, F.; Cherkasov, A. Rapid Identification of Potential Inhibitors of SARS-CoV-2 Main Protease by Deep Docking of 1.3 Billion Compounds. *Mol. Inform.* 2020, *39* (8), 2000028.  
<https://doi.org/10.1002/minf.202000028>.
- (7) Elfiky, A. A. SARS-CoV-2 RNA Dependent RNA Polymerase (RdRp) Targeting: An in Silico Perspective. *J. Biomol. Struct. Dyn.* 2020, 1–9.  
<https://doi.org/10.1080/07391102.2020.1761882>.
- (8) Aftab, S. O.; Ghouri, M. Z.; Masood, M. U.; Haider, Z.; Khan, Z.; Ahmad, A.; Munawar, N. Analysis of SARS-CoV-2 RNA-Dependent RNA Polymerase as a Potential Therapeutic Drug Target Using a Computational Approach. *J. Transl. Med.* 2020, *18* (1), 275. <https://doi.org/10.1186/s12967-020-02439-0>.
- (9) Alexpandi, R.; De Mesquita, J. F.; Pandian, S. K.; Ravi, A. V. Quinolines-Based SARS-CoV-2 3CLpro and RdRp Inhibitors and Spike-RBD-ACE2 Inhibitor for Drug-Repurposing Against COVID-19: An in Silico Analysis. *Front. Microbiol.* 2020, *11*.  
<https://doi.org/10.3389/fmicb.2020.01796>.
- (10) Eastman, R. T.; Roth, J. S.; Brimacombe, K. R.; Simeonov, A.; Shen, M.; Patnaik, S.; Hall, M. D. Remdesivir: A Review of Its Discovery and Development Leading to Emergency Use Authorization for Treatment of COVID-19. *ACS Cent. Sci.* 2020, *6* (5), 672–683. <https://doi.org/10.1021/acscentsci.0c00489>.
- (11) Jin, Z.; Du, X.; Xu, Y.; Deng, Y.; Liu, M.; Zhao, Y.; Zhang, B.; Li, X.; Zhang, L.; Peng, C.; et al. Structure of Mpro from SARS-CoV-2 and Discovery of Its Inhibitors. *Nature* 2020, *582* (7811), 289–293. <https://doi.org/10.1038/s41586-020-2223-y>.
- (12) Hoffmann, M.; Kleine-Weber, H.; Schroeder, S.; Krüger, N.; Herrler, T.; Erichsen, S.; Schiergens, T. S.; Herrler, G.; Wu, N.-H.; Nitsche, A.; et al. SARS-CoV-2 Cell Entry Depends on ACE2 and TMPRSS2 and Is Blocked by a Clinically Proven Protease Inhibitor. *Cell* 2020, *181* (2), 271–280.e8. <https://doi.org/10.1016/j.cell.2020.02.052>.
- (13) Zhang, H.; Penninger, J. M.; Li, Y.; Zhong, N.; Slutsky, A. S. Angiotensin-Converting Enzyme 2 (ACE2) as a SARS-CoV-2 Receptor: Molecular Mechanisms and Potential Therapeutic Target. *Intensive Care Med.* 2020, *46* (4), 586–590.  
<https://doi.org/10.1007/s00134-020-05985-9>.

- (14) Letko, M.; Marzi, A.; Munster, V. Functional Assessment of Cell Entry and Receptor Usage for SARS-CoV-2 and Other Lineage B Betacoronaviruses. *Nat. Microbiol.* 2020, 5 (4), 562–569. <https://doi.org/10.1038/s41564-020-0688-y>.
- (15) Khan, R. J.; Jha, R. K.; Amera, G. M.; Jain, M.; Singh, E.; Pathak, A.; Singh, R. P.; Muthukumaran, J.; Singh, A. K. Targeting SARS-CoV-2: A Systematic Drug Repurposing Approach to Identify Promising Inhibitors against 3C-like Proteinase and 2'-O-Ribose Methyltransferase. *J. Biomol. Struct. Dyn.* 2020, 1–14. <https://doi.org/10.1080/07391102.2020.1753577>.
- (16) Ruch, T. R.; Machamer, C. E. The Coronavirus E Protein: Assembly and Beyond. *Viruses* 2012, 4 (3), 363–382. <https://doi.org/10.3390/v4030363>.
- (17) Gao, Y.; Yan, L.; Huang, Y.; Liu, F.; Zhao, Y.; Cao, L.; Wang, T.; Sun, Q.; Ming, Z.; Zhang, L.; et al. Structure of the RNA-Dependent RNA Polymerase from COVID-19 Virus. *Science (80-. )*. 2020, 368 (6492), 779–782. <https://doi.org/10.1126/science.abb7498>.
- (18) Wu, C.; Liu, Y.; Yang, Y.; Zhang, P.; Zhong, W.; Wang, Y.; Wang, Q.; Xu, Y.; Li, M.; Li, X.; et al. Analysis of Therapeutic Targets for SARS-CoV-2 and Discovery of Potential Drugs by Computational Methods. *Acta Pharm. Sin. B* 2020, 10 (5), 766–788. <https://doi.org/10.1016/j.apsb.2020.02.008>.
- (19) Park, M.; Thwaites, R. S.; Openshaw, P. J. M. COVID-19: Lessons from SARS and MERS. *Eur. J. Immunol.* 2020, 50 (3), 308–311. <https://doi.org/10.1002/eji.202070035>.
- (20) Dong, L.; Hu, S.; Gao, J. Discovering Drugs to Treat Coronavirus Disease 2019 (COVID-19). *Drug Discov. Ther.* 2020, 14 (1), 58–60. <https://doi.org/10.5582/ddt.2020.01012>.
- (21) Castro, A. A.; Assis, L. C.; Ramalho, T. C.; La Porta, F. A. New in Silico Insights into the Application of the (Hydroxy)Chloroquine with Macrolide Antibiotics Co-Crystals against the SARS-CoV-2 Virus. *Research Square* 2020. <https://doi.org/10.21203/rs.3.rs-66640/v1>.
- (22) De Clercq, E. New Nucleoside Analogues for the Treatment of Hemorrhagic Fever Virus Infections. *Chem. Asian J.* 2019, 14 (22), 3962–3968. <https://doi.org/10.1002/asia.201900841>.

- (23) Furuta, Y.; Komeno, T.; Nakamura, T. Favipiravir (T-705), a Broad Spectrum Inhibitor of Viral RNA Polymerase. *Proc. Jpn. Acad. Ser. B. Phys. Biol. Sci.* 2017, 93 (7), 449–463. <https://doi.org/10.2183/pjab.93.027>.
- (24) Mifsud, E. J.; Hayden, F. G.; Hurt, A. C. Antivirals Targeting the Polymerase Complex of Influenza Viruses. *Antiviral Res.* 2019, 169, 104545. <https://doi.org/10.1016/j.antiviral.2019.104545>.
- (25) Jin, Z.; Smith, L. K.; Rajwanshi, V. K.; Kim, B.; Deval, J. The Ambiguous Base-Pairing and High Substrate Efficiency of T-705 (Favipiravir) Ribofuranosyl 5'-Triphosphate towards Influenza A Virus Polymerase. *PLoS One* 2013, 8 (7), e68347. <https://doi.org/10.1371/journal.pone.0068347>.
- (26) Abuo-Rahma, G. E.-D. A.; Mohamed, M. F. A.; Ibrahim, T. S.; Shoman, M. E.; Samir, E.; Abd El-Baky, R. M. Potential Repurposed SARS-CoV-2 (COVID-19) Infection Drugs. *RSC Adv.* 2020, 10 (45), 26895–26916. <https://doi.org/10.1039/D0RA05821A>.
- (27) Kiso, M.; Takahashi, K.; Sakai-Tagawa, Y.; Shinya, K.; Sakabe, S.; Le, Q. M.; Ozawa, M.; Furuta, Y.; Kawaoka, Y. T-705 (Favipiravir) Activity against Lethal H5N1 Influenza A Viruses. *Proc. Natl. Acad. Sci.* 2010, 107 (2), 882 LP – 887. <https://doi.org/10.1073/pnas.0909603107>.
- (28) Furuta, Y.; Takahashi, K.; Shiraki, K.; Sakamoto, K.; Smee, D. F.; Barnard, D. L.; Gowen, B. B.; Julander, J. G.; Morrey, J. D. T-705 (Favipiravir) and Related Compounds: Novel Broad-Spectrum Inhibitors of RNA Viral Infections. *Antiviral Res.* 2009, 82 (3), 95–102. <https://doi.org/https://doi.org/10.1016/j.antiviral.2009.02.198>.
- (29) Cai, Q.; Yang, M.; Liu, D.; Chen, J.; Shu, D.; Xia, J.; Liao, X.; Gu, Y.; Cai, Q.; Yang, Y.; et al. Experimental Treatment with Favipiravir for COVID-19: An Open-Label Control Study. *Engineering* 2020. <https://doi.org/https://doi.org/10.1016/j.eng.2020.03.007>.
- (30) Harismah, K.; Mirzaei, M. Favipiravir: Structural Analysis and Activity against COVID-19. *Adv. J. Chem. B* 2020, 2 (2), 55–60. <https://doi.org/10.33945/SAMI/AJCB.2020.2.3>.
- (31) Mendes, J.; de Almeida, K. J.; Neto, J. L.; Ramalho, T. C.; Duarte, H. A. Theoretical Spectroscopic Insights of Tautomers and Enantiomers of Penicillamine. *Spectrochim. Acta Part A Mol. Biomol. Spectrosc.* 2017, 184, 308–317.

<https://doi.org/https://doi.org/10.1016/j.saa.2017.05.025>.

- (32) Timm, R. A.; Bonacin, J. A.; Formiga, A. L. B.; Toma, H. E. A Theoretical Study of the Tautomerism and Vibrational Spectra of 4,5-Diamine-2,6-Dimercaptopyrimidine. *J. Braz. Chem. Soc.* 2008, *19*, 287–292.
- (33) Erdoğan, Ş.; Işın, D. Ö. Theoretical Study on the Self- and Water-Assisted Proton Transfer Reaction of Urazole. *Chem. Heterocycl. Compd.* 2014, *50* (7), 986–997. <https://doi.org/10.1007/s10593-014-1554-8>.
- (34) Pliego, J.; Rufino, V. Mechanisms of the Formation of Imines in Aqueous Solution and the Effect of the PH: A Theoretical Analysis. *Arkivoc* 2020, 2020. <https://doi.org/10.24820/ark.5550190.p011.105>.
- (35) Puzzarini, C.; Barone, V. Diving for Accurate Structures in the Ocean of Molecular Systems with the Help of Spectroscopy and Quantum Chemistry. *Acc. Chem. Res.* 2018, *51* (2), 548–556. <https://doi.org/10.1021/acs.accounts.7b00603>.
- (36) Shi, F.; Li, Z.; Kong, L.; Xie, Y.; Zhang, T.; Xu, W. Synthesis and Crystal Structure of 6-Fluoro-3-Hydroxypyrazine-2-Carboxamide. *Drug Discov. Ther.* 2014, *8* (3), 117–120. <https://doi.org/10.5582/ddt.2014.01028>.
- (37) Rhyman, L.; Tursun, M.; Abdallah, H. H.; Choong, Y. S.; Parlak, C.; Kharkar, P.; Ramasami, P. Theoretical Investigation of the Derivatives of Favipiravir (T-705) as Potential Drugs for Ebola Virus. *Phys. Sci. Rev.* 3 (9), 20170198. <https://doi.org/https://doi.org/10.1515/psr-2017-0198>.
- (38) Sahoo, H. Förster Resonance Energy Transfer – A Spectroscopic Nanoruler: Principle and Applications. *J. Photochem. Photobiol. C Photochem. Rev.* 2011, *12* (1), 20–30. <https://doi.org/10.1016/j.jphotochemrev.2011.05.001>.
- (39) Sedgwick, A. C.; Wu, L.; Han, H.-H.; Bull, S. D.; He, X.-P.; James, T. D.; Sessler, J. L.; Tang, B. Z.; Tian, H.; Yoon, J. Excited-State Intramolecular Proton-Transfer (ESIPT) Based Fluorescence Sensors and Imaging Agents. *Chem. Soc. Rev.* 2018, *47* (23), 8842–8880. <https://doi.org/10.1039/C8CS00185E>.
- (40) Zamyatkin, D. F.; Parra, F.; Machín, A.; Grochulski, P.; Ng, K. K.-S. Binding of 2'-Amino-2'-Deoxycytidine-5'-Triphosphate to Norovirus Polymerase Induces Rearrangement of the Active Site. *J. Mol. Biol.* 2009, *390* (1), 10–16.

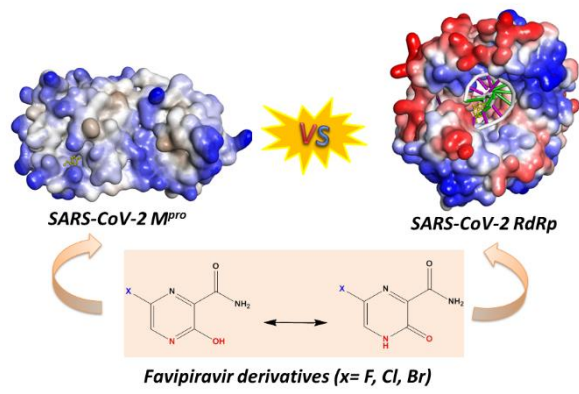
<https://doi.org/10.1016/j.jmb.2009.04.069>.

- (41) Berman, H. M.; Westbrook, J.; Feng, Z.; Gilliland, G.; Bhat, T. N.; Weissig, H.; Shindyalov, I. N.; Bourne, P. E. The Protein Data Bank. *Nucleic Acids Res.* 2000, 28 (1), 235–242. <https://doi.org/10.1093/nar/28.1.235>.
- (42) Maia, E. H. B.; Medaglia, L. R.; da Silva, A. M.; Taranto, A. G. Molecular Architect: A User-Friendly Workflow for Virtual Screening. *ACS omega* 2020, 5 (12), 6628–6640. <https://doi.org/10.1021/acsomega.9b04403>.
- (43) Trott, O.; Olson, A. J. AutoDock Vina: Improving the Speed and Accuracy of Docking with a New Scoring Function, Efficient Optimization, and Multithreading. *J. Comput. Chem.* 2010, 31 (2), 455–461. <https://doi.org/10.1002/jcc.21334>.
- (44) Yang, H.; Yang, M.; Ding, Y.; Liu, Y.; Lou, Z.; Zhou, Z.; Sun, L.; Mo, L.; Ye, S.; Pang, H.; et al. The Crystal Structures of Severe Acute Respiratory Syndrome Virus Main Protease and Its Complex with an Inhibitor. *Proc. Natl. Acad. Sci. U. S. A.* 2003, 100 (23), 13190–13195. <https://doi.org/10.1073/pnas.1835675100>.
- (45) Lipinski, C. A.; Lombardo, F.; Dominy, B. W.; Feeney, P. J. Experimental and Computational Approaches to Estimate Solubility and Permeability in Drug Discovery and Development Settings. *Adv. Drug Deliv. Rev.* 1997, 23 (1), 3–25. [https://doi.org/https://doi.org/10.1016/S0169-409X\(96\)00423-1](https://doi.org/https://doi.org/10.1016/S0169-409X(96)00423-1).
- (46) M. J. Frisch, G. W. Trucks, H. B. Schlegel, G. E. Scuseria, M. A. Robb, J. R. Cheeseman, G. Scalmani, V. Barone, G. A. Petersson, H. Nakatsuji, X. Li, M. Caricato, A. Marenich, J. Bloino, B. G. Janesko, R. Gomperts, B. Mennucci, H. P. Hratchian, J. V. Ort, W. C. Gaussian, Inc., Wallingford CT. 2009.
- (47) Miertuš, S.; Scrocco, E.; Tomasi, J. Electrostatic Interaction of a Solute with a Continuum. A Direct Utilizaion of AB Initio Molecular Potentials for the Prevision of Solvent Effects. *Chem. Phys.* 1981, 55 (1), 117–129. [https://doi.org/https://doi.org/10.1016/0301-0104\(81\)85090-2](https://doi.org/https://doi.org/10.1016/0301-0104(81)85090-2).
- (48) Miertuš, S.; Tomasi, J. Approximate Evaluations of the Electrostatic Free Energy and Internal Energy Changes in Solution Processes. *Chem. Phys.* 1982, 65 (2), 239–245. [https://doi.org/10.1016/0301-0104\(82\)85072-6](https://doi.org/10.1016/0301-0104(82)85072-6).
- (49) London, F. Théorie Quantique Des Courants Interatomiques Dans Les Combinaisons

Aromatiques. *J. Phys. le Radium* 1937, 8 (10), 397–409.

<https://doi.org/10.1051/jphysrad:01937008010039700>.

- (50) McWeeny, R. Perturbation Theory for the Fock-Dirac Density Matrix. *Phys. Rev.* 1962, 126 (3), 1028–1034. <https://doi.org/10.1103/PhysRev.126.1028>.
- (51) Ditchfield, R. Self-Consistent Perturbation Theory of Diamagnetism. *Mol. Phys.* 1974, 27 (4), 789–807. <https://doi.org/10.1080/00268977400100711>.
- (52) Wolinski, K.; Hinton, J. F.; Pulay, P. Efficient Implementation of the Gauge-Independent Atomic Orbital Method for NMR Chemical Shift Calculations. *J. Am. Chem. Soc.* 1990, 112 (23), 8251–8260. <https://doi.org/10.1021/ja00179a005>.
- (53) Cheeseman, J. R.; Trucks, G. W.; Keith, T. A.; Frisch, M. J. A Comparison of Models for Calculating Nuclear Magnetic Resonance Shielding Tensors. *J. Chem. Phys.* 1996, 104 (14), 5497–5509. <https://doi.org/10.1063/1.471789>.
- (54) Grimme, S. Towards First Principles Calculation of Electron Impact Mass Spectra of Molecules. *Angew. Chemie Int. Ed.* 2013, 52 (24), 6306–6312. <https://doi.org/10.1002/anie.201300158>.
- (55) Koopman, J.; Grimme, S. Calculation of Electron Ionization Mass Spectra with Semiempirical GFNn-XTB Methods. *ACS Omega* 2019, 4 (12), 15120–15133. <https://doi.org/10.1021/acsomega.9b02011>.
- (56) Hanwell, M. D.; Curtis, D. E.; Lonie, D. C.; Vandermeersch, T.; Zurek, E.; Hutchison, G. R. Avogadro: An Advanced Semantic Chemical Editor, Visualization, and Analysis Platform. *J. Cheminform.* 2012, 4 (1), 17. <https://doi.org/10.1186/1758-2946-4-17>.
- (57) Webb, B.; Sali, A. Comparative Protein Structure Modeling Using MODELLER. *Curr. Protoc. Bioinforma.* 2016, 54, 5.6.1-5.6.37. <https://doi.org/10.1002/cpbi.3>.
- (58) Novoselov, K. P.; Shirabaikin, D. B.; Umanskii, S. Y.; Vladimirov, A. S.; Minushev, A. K.; Korin, A. A. CHIMERA: A Software Tool for Reaction Rate Calculations and Kinetics and Thermodynamics Analysis. *J. Comput. Chem.* 2002, 23 (14), 1375–1389. <https://doi.org/10.1002/jcc.10105>.
- (59) Accelrys Software. Discovery Studio Modeling Environment. San Diego 2012.



**Graphic Abstract.**